Deformation and Interfacial Sliding in Back-End Interconnect Structures in Microelectronic Devices

C. PARK,[1] I. DUTTA,[1,3] K.A. PETERSON,[1] and J. VELLA[2]

1.—Center for Materials Science and Engineering, Department of Mechanical Engineering, Naval Postgraduate School, Monterey, CA 93943. 2.—Process and Materials Characterization Laboratory, Motorola, Tempe, AZ 85284. 3.—E-mail: idutta@nps.navy.mil

Deformation of interconnect structures at the back-end of microelectronic devices during processing or service can have a pronounced effect on component reliability. Here, we use atomic force microscopy (AFM) to study plastic deformation and interfacial sliding of Cu interconnects on Si. The behavior of both standalone Cu lines and lines embedded in a low-K dielectric (LKD) was studied. Following thermal cycling, changes were observed in the in-plane (IP) Cu line dimensions, as well as the out-of-plane (OOP) step height between Cu and the dielectric in single-layer structures. These were attributed to differential deformation of the Cu/Si and Cu/dielectric material pairs caused by thermal expansion mismatch, accommodated by interfacial creep. These results are discussed in light of previous work on the mechanism of interfacial creep. A simple shear-lag-based model, which may be used to estimate the extent of interfacial sliding, is proposed. Some experimental results on the distortion of Cu lines caused by package-level stresses following thermal cycling are also presented.

Key words: Copper interconnects, low-K dielectric, deformation, interfacial sliding, thermal cycling

DRAFT

INTRODUCTION

The large mismatch in the coefficients of thermal expansion (CTE) between metallic thin films and Si substrates usually causes plasticity and creep of the film during thermal cycling.[1] This mismatch also generates shear stresses at the interface, which can drive diffusionally accommodated interfacial sliding, resulting in alteration of the film footprint on the substrate.[2–4] In large area films, these shear stresses (and, hence, sliding) are limited to regions close to the film edges; but for films with small lateral dimensions (e.g., narrow interconnect lines), sliding may occur over a large area fraction of the interface. In Al/SiO_2 back-end interconnect structures (BEIS), sliding and the associated line-dimension changes are constrained by the stiff SiO_2 dielectric. However, with the increasing use of mechanically compliant dielectrics with low dielectric constant (K) in the back ends of modern microelectronic devices, changes in line dimensions caused by plasticity and sliding are unlikely to be fully constrained. This is particularly exacerbated by far-field shear stresses imposed on the BEIS caused by joining of the device to a package-level substrate (typically an organic material with a much higher CTE than Si). Under the joint action of the local (film/Si level) and global (Si/package level) stresses, the film can yield incrementally during each thermal cycle, resulting in crawling of the film on the substrate in the direction of the global shear stress.[5] Under interfacial sliding conditions, crawling is likely to be exaggerated, particularly when thesurrounding low-K dielectric (LKD) is unable to provide sufficient mechanical constraint, possibly resulting in shifting line positions and large-scale line distortions. In addition to occurring along the in-plane (IP) Cu/Si interfaces, sliding also occurs at vertical Cu/LKD interfaces because of the out-of-plane (OOP) CTE mismatch between Cu and LKD, causing steps to appear at these interfaces.[6,7]

(Received May 30, 2003; accepted June 25, 2003)

In this paper, we present results of atomic force microscope (AFM) measurements of both lateral and OOP dimensions of (a) standalone Cu lines on Si and (b) Cu/LKD structures on Si with the intent of delineating the role of interfacial sliding during thermal cycling of devices during processing and service. We also present a model, based on shear lag at the interface, which can predict the extent of interfacial sliding at film/substrate interfaces during thermal cycling. Some preliminary observations of deformation of back-end structures caused by global package-level loads are also reported.

EXPERIMENTAL APPROACH

A heating stage was constructed for a commercial AFM, and the piezoelectric scanning device of the AFM was carefully insulated thermally to minimize image distortion. This AFM was used for in-situ studies of back-end structures on Si (sample details follow later) during thermal cycling from 293 K to 398 K. The AFM was enclosed in a bell-jar vacuum system, which was pumped down to 5×10^{-2} torr, followed by backfilling with forming gas (98% argon, 2% hydrogen) to a final chamber pressure of ~1 torr. This prevented oxidation of the sample during cycling and enhanced the thermal stability of the AFM. Following addition of the hot stage, the calibration of the AFM was checked using a Si sample containing 1-μm-wide surface grooves with a pitch of 3 μm, based on which the IP CTE of Si was determined over 293–398 K. The measured IP CTE of 3×10^{-6}/K agreed well with the reference CTE for Si (2.8×10^{-6}/K), validating the calibration. In ddition to the in-situ hot-stage studies, the AFM was used to investigate deformation and sliding of BEIS at ambient temperature following ex-situ thermal cycling.

Three types of samples were used for the AFM experiments. The first type (A) comprised a pattern of parallel 1.4-μm-wide, 250-nm-thick, electroplated Cu lines with a pitch of 2 μm on Si with a 35-nm Ta barrier layer at the interface, as shown in Fig. 1. This sample was used to study deformation and sliding of standalone Cu lines on Si along both IP and out-of plane (OOP) directions. The second sample type (B) consisted of one layer of 350-nm-thick, alternating parallel Cu and LKD lines on Si, as shown in Fig. 2. The width of the Cu lines, which were surrounded on the sides and bottom by a 35-nm-thick Ta barrier layer, varied from 0.2 μm to 1.8 μm, with the corresponding LKD width ranging from 1.4 μm to 1.1 μm. This sample, fabricated via the damascene process using a hybrid organic/inorganic silicate-based LKD with a k value of approximate 2.5 and chemomechanically polished (CMP) to produce a nominally flat surface, was used to study deformation and sliding along the OOP direction. Both samples (A and B) were annealed for 30 min at 673 K after Cu electroplating, producing Cu lines that were nearly stress free at 293 K.[8] Both samples A and B were subjected to five ex-situ thermal cycles from 293 K to 723 K in vacuum (10^{-6} torr) at nominal heating and cooling rates of 10 K/min, and the surface profiles were measured perpendicular to the Cu line length before and after each cycle by an AFM at 293 K. Sample B was also cycled in-situ in the AFM from 293 K to 398 K, and the profiles were recorded at selected temperatures.

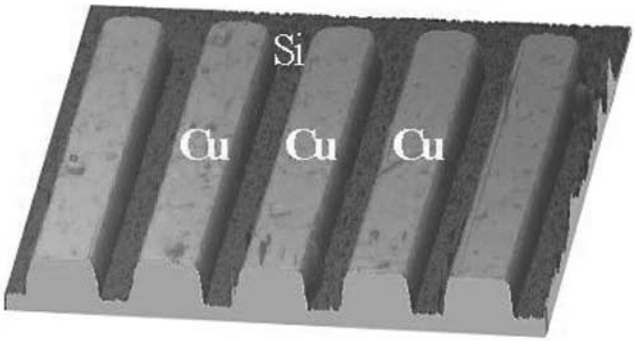

Fig. 1. An AFM image of a pattern of parallel 1.4-μm wide, 250-nm thick, electroplated Cu lines with a pitch of 2 μm on Si with a 35-nm Ta barrier layer at the Cu/Si interface (sample type A).

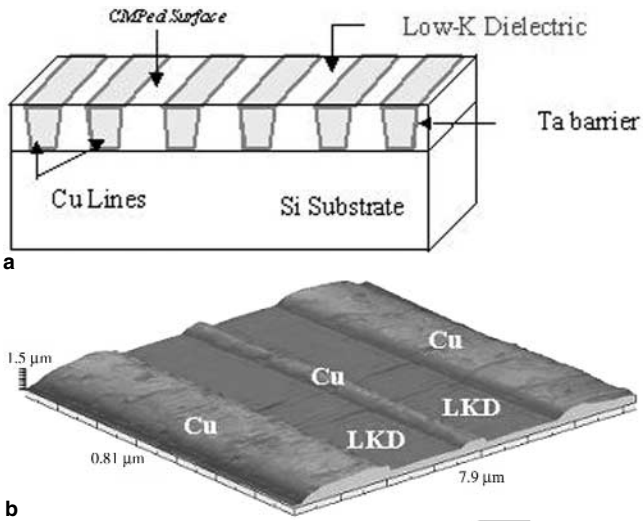

Fig. 2. (a) A schematic of the cross section of sample B, showing a single-layer Cu/LKD interconnect structure. The structure consists of one layer of 350-nm thick, alternating parallel Cu and LKD lines of different widths on a Si substrate. (b) Surface AFM image of the Cu/LKD structure after CMP.

In a few of the samples of type B, the Cu lines were etched off completely by immersion in a solution of 3 g/L of sodium persulfate ($Na_2S_2O_8$) in 2% H_2SO_4, leaving the LKD lines unaffected. Although the etching did not remove the 35-nm Ta barrier layer, this layer provides negligible constraint on the LKD deformations and, therefore, is not expected to influence to measured CTE data. These samples were used to measure the IP CTE of the LKD material by measuring the cross-sectional line profiles at different temperatures. Figure 3 shows an AFM image of the sample following etching of the Cu, as well as the cross-sectional AFM profile of an LKD line

DRAFT

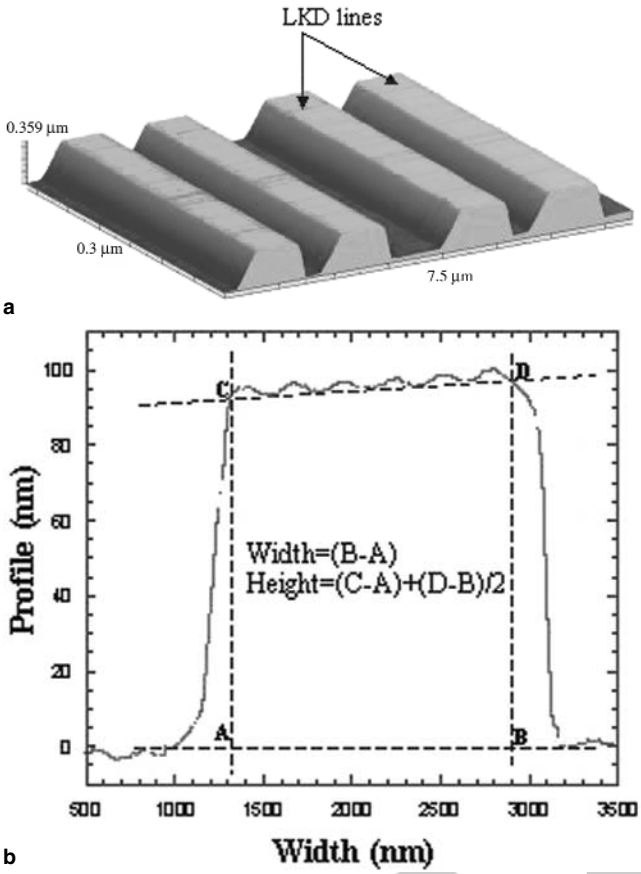

Fig. 3. (a) An AFM image of the single-layer Cu/LKD sample, following etching of the Cu lines, showing only LKD lines on Si. (b) AFM line scan of the profile of an LKD line, showing the parameters used to determine the IP CTE of LKD.

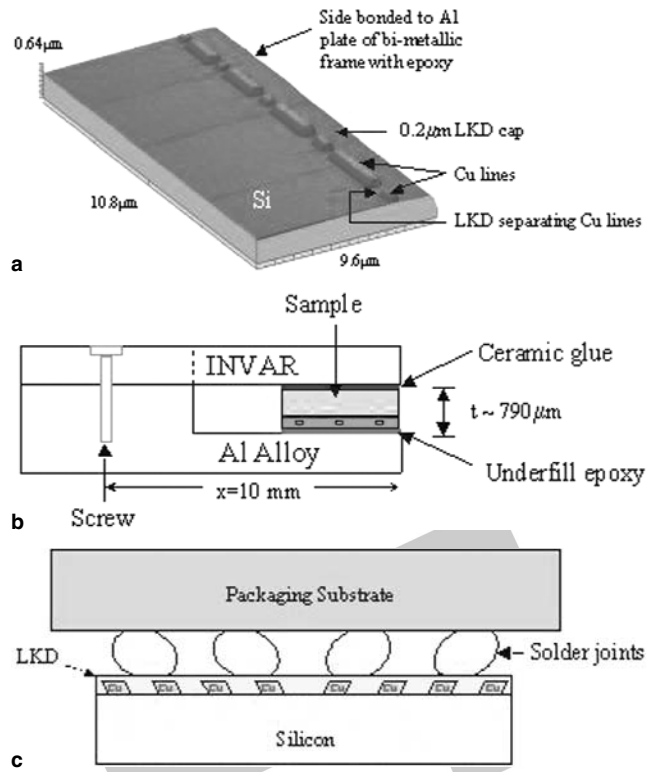

Fig. 4. (a) An AFM image of the microcleaved and FIB-polished cross section of sample C, showing alternating 0.5-µm and 1.8-µm Cu lines embedded in LKD on Si. (b) Schematic of the bimetallic fixture constructed of Invar and Al, on which sample C was mounted for simulating shear deformation of the back-end structure caused by package-level stresses during thermal cycling. (c) Schematic of expected deformation of the BEIS caused by the CTE mismatch between Si and the substrate in flip-chip packaging. Note that if the LKD material is compliant relative to the solder, substantial shear strains may be induced in the BEIS; the strain increasing with increasing distance from the centerline.

along with the parameters used to determine the CTE. Because dimensions of the LKD line near the bottom (i.e., the line/substrate interface) are affected by thermally induced IP stresses (σ^{OP}_{LKD}) caused by CTE mismatch between LKD and Si, the LKD line width was measured by identifying the points C and D at the top edges of the line profile and projecting them on the substrate to obtain the dimension AB with the assumption that at the top surface of the LKD line, $\sigma^{IP}_{LKD} \approx 0$. At least 50 separate profiles obtained from the same line were measured, and the mean line width at a given temperature was determined from the distribution. The IP CTE of the LKD was then determined from the slope of the mean line width versus temperature plot. In principle, the OOP CTE is also determinable from the same experiments. However, for the 350-nm thickness of the present LKD lines, the OOP expansion of the line caused by a 100-K temperature change would only be ~0.175–0.7 nm for a CTE range of 5×10^{-6}/K to 20×10^{-6}/K. Because the OOP resolution of most AFMs is limited to about 1% of the total OOP displacement range, in this case, no less than a 3.5-nm OOP displacement would be measurable with confidence. Therefore, only the CTE in the IP direction was measured in the present work.

A third type of sample (C) comprised a single layer of 350-nm-thick, alternating Cu/LKD lines, capped by a 2,000-nm LKD layer. The sample cross section was revealed by microcleaving normal to the interconnect lines, followed by focused ion beam (FIB) polishing. An AFM image of the sample cross section, showing alternating 0.5-µm and 1.8-µm Cu lines embedded in LKD on Si, is shown in Fig. 4a. The sample was mounted in a bimetallic fixture constructed of Invar and Al, as shown in Fig. 4b. The LKD side of the sample was bonded to the Al plate (CTE = 22×10^{-6}/K) using a glass-filled epoxy used for underfilling flip-chip packages (E = 11 GPa, CTE = 21×10^{-6}/K), whereas the Si side was bonded to the Invar plate (CTE = 0.5×10^{-6}/K) using a ceramic glue. During thermal cycling, this arrangement allowed the BEIS to be placed in severe shear caused by the CTE mismatch between Al and Invar. At any temperature, T, the nominal maximum shear strain imposed on the chip is given by $\Delta\alpha\Delta T \cdot x/t$, where $\Delta\alpha$ is the CTE difference between Al and Invar, ΔT is the difference between T and the ambient temperature, x (10 mm) is the effective length of the bimetallic fixture, and t (~793 µm) is

DRAFT

nominally the sum of the thicknesses of the chip (t_{chip} = 753 μm) and the glue layers ($t_{ceramic\ glue}$ + $t_{underfill}$ ~ 40 μm). In actuality, because the ceramic glue and Si are relatively stiff, the majority of the imposed shear deformation is likely to be concentrated in the compliant low-K layer and underfill epoxy (which have low Young's moduli of 5–7 GPa and 11 GPa, respectively). This allows the local shear strain within the Cu/low-K BEIS to be very large. For ΔT = 100 K, the shear strain in the BEIS may be estimated to be on the order of $\Delta\alpha\Delta T\, x/(t_{BEIS} + t_{underfill})$, which is ~0.5–1. This setup was used to perform both in-situ thermal cycling experiments (293–398 K) in the AFM, as well as ex-situ cycling in a vacuum chamber (10^{-5} torr), followed by observation of the sample cross sections in the AFM. These experiments allowed simulation of BEIS deformation caused by the CTE mismatch between Si and the substrate in flip-chip packaging, which is shown schematically in Fig. 4c. For a 20-μm-square Si device attached to an FR-4™ substrate (CTE = 18×10^{-6}/K) with flip-chip solder joints of 50-μm height, the shear strain imposed on the solder joints and the BEIS together is ~0.4 for a temperature differential of 100 K. Although for stiff BEIS with oxide dielectrics, this strain would be accommodated almost entirely by deformation of the solder (E ~ 25 GPa at 298 K), for compliant BEIS with LKDs (E ~ 5 GPa), much of this shear displacement would be within the BEIS, resulting in shear strains substantially greater than the nominal value of ~0.4. Thus, the experiments reported here provide an effective means of simulating back-end deformation during thermal cycling.

MODEL

Here, we outline a simple micromechanical model to capture the observed OOP deformation and sliding at Cu/LKD interfaces in a single-layer BEIS by representing the BEIS as shown in Fig. 5. Although sliding actually occurs at Cu/Ta interfaces, the Ta layer is too thin to affect the stress states in Cu and LKD and may, therefore, be ignored in the model. It is further assumed that the narrow lines do not cause significant substrate curvature about the Y axis (i.e., on the XZ plane), and because the lines are long, we have a nominally plane-strain condition with $\varepsilon_{yy} \approx 0$. The LKD is assumed to be elastic, and the Cu is elastic-linear plastic and can creep via diffusional creep.* Because of the CTE mismatch between Cu and LKD in the OOP direction, a shear lag develops at the Cu/LKD interfaces when the structure is subjected to a thermal excursion. This shear lag[10,11] results in a spatially varying interfacial shear stress (τ_i), which can drive diffusionally accommodated interfacial sliding.

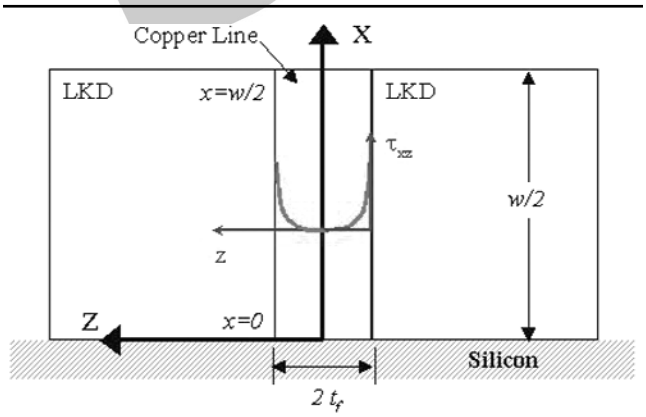

Fig. 5. A schematic of a single-layer Cu/LKD BEIS with the relevant parameters for the OOP sliding and deformation model. The lengths of the Cu and LKD lines are along the Y axis, which is normal to the plane of the paper. The distribution of the shear stress τ_{xz} across the width (z direction) of the Cu line is also shown schematically.

The mechanism of diffusionally accommodated interfacial sliding has been studied in detail by Funn and Dutta[12] and Peterson et al.[13,14] It is now established that interfacial sliding occurs via diffusional creep with a basic mechanism akin to that of grain boundary sliding,[15] where an applied far-field stress causes local normal-stress gradients at the interface because of topographical variations, allowing mass transport and, hence, sliding along the interface. The resulting shear-strain rate is given by

$$\dot{\bar{\gamma}}_i = \frac{4\delta_i D_{io}\Omega}{kTh^3}\left[\tau_i + 2\pi^3\left(\frac{h}{\lambda}\right)^3 \sigma_n\right] e^{-\frac{Q_i}{RT}} \qquad (1)$$

where δ_i is the interfacial thickness; D_{io} and Q_i are the frequency factor and activation energy for interfacial diffusion, respectively; Ω is the atomic volume of the diffusing species (Cu in the present case); λ and h are the topographical periodicity and roughness of the interface respectively; and k, R, and T are Boltzmann's constant, the universal gas constant, and temperature, respectively. The interfacial shear stress, τ_i, is the primary driving force for this process, which is enhanced if a tensile normal-interfacial stress, σ_n, is present or reduced if there is a compressive σ_n. Because $\dot{\bar{\gamma}}i \propto h^{-3}$, a smooth interface would slide more readily, explaining the preponderance of this phenomenon in the ultra-smooth interfaces in microelectronic devices (e.g., Cu/Ta). The sliding kinetics are further enhanced by the low value of Q_i, which is typically significantly lower than that for grain boundary diffusion in the less refractory side of the interface.[12–14,16]

Here, we use a modification of the shear-lag theory[10,11] to determine τ_i as a function of x and then use the result to compute the differential deformation of Cu and LKD in the OOP direction by allowing the interface to slide using an approach similar to Ref. 17. We assume that the shear stress, τ_{xz},

* Dislocation creep is ignored because dislocation activity is typically limited in thin films as a result of constraints imposed by surface layers, such as passivation or barrier layers.[9]

DRAFT

in the Cu film is maximum at the interface (i.e., at $z = 0$, $\tau_{xz} = \tau_i$) and, because of symmetry, equals zero at the middle of the line width (i.e., at $z = t_f$, $\tau_{xz} = 0$), decaying exponentially with z. Thus, τ_{xz} may be represented as

$$\tau_{xz} = \tau_i \exp(-B \cdot z/t_f) \tag{2}$$

Representing the conditions of equilibrium within the film as

$$\frac{\partial \sigma_x}{\partial x} + \frac{\partial \tau_{xz}}{\partial z} = 0, \quad \frac{\partial \tau_{xz}}{\partial x} + \frac{\partial \sigma_z}{\partial z} = 0 \tag{3}$$

we can adapt the approach of Ref. 17 to compute τ_i and the normal interfacial stress ($\sigma_n = \sigma_z$ at $z = 0$) as a function of x by using the shear-lag theory. When the temperature excursion, ΔT, is small enough that the yield strength of the Cu line is not exceeded, (i.e., for $\sigma_x < \sigma_{YS}$), this gives

$$\tau_i = \frac{t_f}{B} \frac{\Delta\alpha \Delta T \cdot \beta}{P \cosh(\beta \frac{w}{2})} \sinh(\beta x) \tag{4a}$$

$$\sigma_n = -\left(\frac{t_f}{B}\right)^2 \left(1 - e^{-B}\right) \beta^2 \frac{\Delta\alpha \Delta T \cdot \beta}{P \cosh(\beta \frac{w}{2})} \cosh(\beta x) \tag{4b}$$

where $2t_f$ is the line width, w/2 is the line thickness, $\Delta\alpha$ is the CTE mismatch between Cu and LKD, and P and β are material constants, given by

$$\beta = \sqrt{H P}$$

where

$$H = \frac{B}{t_f [N + M]}, \quad N = \left(\frac{1}{G_f} + A''\right) \frac{t_f}{B} (1 - e^{-B}),$$
$$M = h A_i t, \text{ and } P = \frac{1}{E_f} + \frac{A''}{3} \tag{5a}$$

Here, E_f and G_f are the Young's modulus and shear modulus of the Cu film, t is time, and A'' is the diffusional creep constant for Cu such that the shear creep rate of Cu is

$$\dot{\gamma}_f^{creep} = A'' \tau_{xz} \text{ and } A'' = \frac{14\Omega}{3kTd^2}\left[D_L + \left(\frac{\pi}{d}\right)\delta_{gb} D_{gb}\right] \tag{5b}$$

where D_L, D_{gb}, d, and δ_{gb} are the lattice diffusivity, grain boundary diffusivity, grain size, and grain boundary thickness of Cu. In Eq. 5a, A_i is the creep constant for the interface, given by

$$A_i = \frac{4\delta_i D_{i0} \Omega}{kTh^3} \exp\left(\frac{-Q_i}{RT}\right) \tag{5c}$$

When the Cu line has yielded because of OOP deformation (i.e., for $\sigma_x > \sigma_{YS}$),

$$\tau_i = \frac{t_f}{B} \frac{(\Delta\alpha\Delta T - P'') \cdot \beta'}{P' \cosh(\beta' \frac{w}{2})} \sinh(\beta' x) \tag{6a}$$

$$\text{and } \sigma_n = -\left(\frac{t_f}{B}\right)^2 \left(1 - e^{-B}\right) \beta'^2 \frac{(\Delta\alpha\Delta T - P'') \cdot \beta'}{P' \cosh(\beta' \frac{w}{2})} \cosh(\beta' x) \tag{6b}$$

$$\text{where } \beta' = \sqrt{H' P'}, \; P' = \frac{1}{E_f} + \frac{A''}{3} + \frac{1}{3K''},$$
$$P'' = \sigma_{YS}/3K'', \; H' = \frac{B}{t_f [N' + M]},$$

$N' = \left(\frac{1}{G_f} + A'' + \frac{1}{K''}\right) \frac{T_f}{B}(1 - e^{-B})$, and K'' is the linear hardening (plastic) modulus of the Cu film in shear.

After computing τ_i and σ_n using Eq. 4 or 6, we apply the condition of stress equilibrium along the OOP (i.e., x) direction under conditions of differential OOP deformation of Cu and LKD (i.e., $\bar{\varepsilon}_f \neq \bar{\varepsilon}_s$). At any value of x, this requires that

$$\bar{\sigma}_f t_f + \bar{\sigma}_s t_s \left[\frac{1 + \bar{\varepsilon}_f}{1 + \bar{\varepsilon}_s}\right] = 0 \tag{7}$$

where $\bar{\sigma}_f$ and $\bar{\sigma}_s$ are the average OOP stress in Cu and LKD, respectively, and t_f and t_s are the half-widths of the Cu and LKD lines (Fig. 6). Further, we apply the condition of strain continuity at the interface at the free surface (i.e., at $x = w/2$), where the interfacial shear strain, γ_i, is at its maximum value and determines the difference between the mean OOP strains in the adjoining Cu ($\bar{\varepsilon}_f$) and LKD ($\bar{\varepsilon}_s$) lines as follows:

$$\frac{w_f}{2}\left(\bar{\varepsilon}_f - \bar{\varepsilon}_s\right) = h\,\gamma_i \tag{8}$$

$$\text{where } \gamma_i = \dot{\bar{\gamma}}_i (x = w/2)\, t = A_i \left[\tau_i (x = w/2) - 2\pi^3 \left(\frac{h}{\lambda}\right)^3 \sigma_n (x = w/2)\right] t \tag{9a}$$

$$\bar{\varepsilon}_f = \bar{\varepsilon}_f^{thermal} + \bar{\varepsilon}_f^{elastic} + \bar{\varepsilon}_f^{plastic} + \bar{\varepsilon}_f^{creep} \tag{9b}$$

$$\bar{\varepsilon}_s = \bar{\varepsilon}_s^{thermal} + \bar{\varepsilon}_s^{elastic} \tag{9c}$$

In Eq. 9a–c, the various strain components for a given material j (where j = f or s for Cu or LKD, respectively) are given by

$$\bar{\varepsilon}_j^{thermal} = \int_{T_1}^{T_2} \alpha_j \, dT, \quad \bar{\varepsilon}_j^{elastic} = \frac{\bar{\sigma}_j}{E_j},$$
$$\bar{\varepsilon}_f^{plastic} = \frac{\bar{\sigma}_f - \sigma_{YS}}{3K''}, \text{ and } \bar{\varepsilon}_f^{creep} = 3A'' \bar{\sigma}_f \tag{10}$$

where $\bar{\sigma}_j$ is the average stress in material j along the x direction. Although σ_j and ε_j vary along the x direction, for analytical expediency, our model uses average stress/strain values.

Now, writing Eq. 7 in the incremental form and substituting for $\bar{\varepsilon}_f$ and $\bar{\varepsilon}_s$ using Eqs. 9a–c and 10, we have, for the average OOP stress increment in Cu caused by temperature change, ΔT, in time increment, Δt:

DRAFT

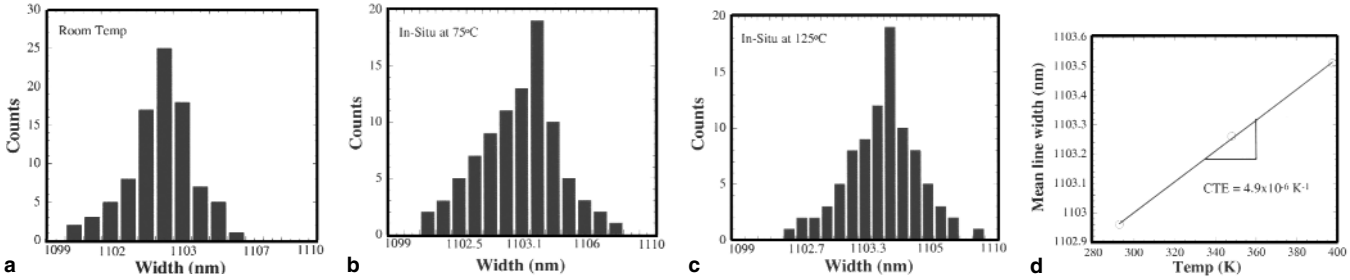

Fig. 6. (a)–(c) The histograms of the width distribution of LKD lines at different temperatures and (d) the variation of the mean line width with temperature. The slope of the mean line width versus temperature plot represents the IP CTE of the LKD.

$$\Delta\bar{\sigma}_f = -\left[\frac{\Delta\alpha\Delta T + \Delta\varepsilon_f^{cr} - \frac{2h}{w}A_i\Delta t\left[\tau_i\left(x=\frac{w}{2}\right) - 2\pi^3\left(h/\lambda\right)^3\sigma_n\left(x=\frac{w}{2}\right)\right]}{\frac{t_f}{E_s t_s}\left(\frac{1+\bar{\varepsilon}_f}{1+\bar{\varepsilon}_s}\right) + \frac{1}{E_f} + \frac{1}{3K''}}\right] \quad (11)$$

The basic solution procedure to obtain the OOP stress/strain states of the Cu and LKD lines during a thermal excursion consists of (1) calculating the initial Cu stress state, σ_{f_o}, at the start of the thermal excursion; (2) calculating the incremental stress change, $\Delta\sigma_f$, using Eq. 11; (3) updating the Cu stress as $\bar{\sigma}_{f_n} = \bar{\sigma}_{f_{n-1}} + \Delta\bar{\sigma}_f$ (here, the subscript n represents the nth solution step); and then (4) computing the Cu and LKD strain components using Eq. 9a–c. This procedure is used iteratively, allowing the temperature or time to change incrementally. At each solution step, the stress and strain increments are calculated, and the Cu and LKD stress/strain are updated. This was achieved using a computer program written in the MATLAB™ programming language.

RESULTS AND DISCUSSION

Coefficient of Thermal Expansion of the Low-K Dielectric

Figure 6a–c shows histograms of the LKD line-width distribution measured from AFM line profiles of the samples with etched-off Cu lines at 293 K, 348 K, and 398 K. The widths display a nominally Gaussian distribution at all three temperatures. Quite clearly, the mean of the distribution increases with increasing temperature; the variation of the mean line width with temperature being shown in Fig. 6d. From the slope of the plot in Fig. 6d, the IP CTE of the LKD was determined to be 4.9×10^{-6}/K, which is significantly lower than that of Cu.

Sliding at In-Plane Cu/Ta/Si Interfaces

Figure 7a shows typical profiles of a standalone Cu line (sample A) prior to and following the first through fifth cycle between 293 K and 723 K. Statistical analysis of 50–100 such line profiles for each condition revealed that the Cu lines shrank laterally with progressive cycling, along with a corresponding increase in line thickness (height), as observed in Fig. 7b, which also shows that the rate of these changes slowed with progressive cycling. Finite element modeling[3] has shown that during the first cycle, heating induces IP compressive stresses in Cu, producing compressive inelastic strains over 450–723 K. During cooling, tensile plasticity occurs below ~400 K, and the film is placed in tension at 293 K, consistent with experiments.[18] The net permanent strain per cycle, however, is compressive

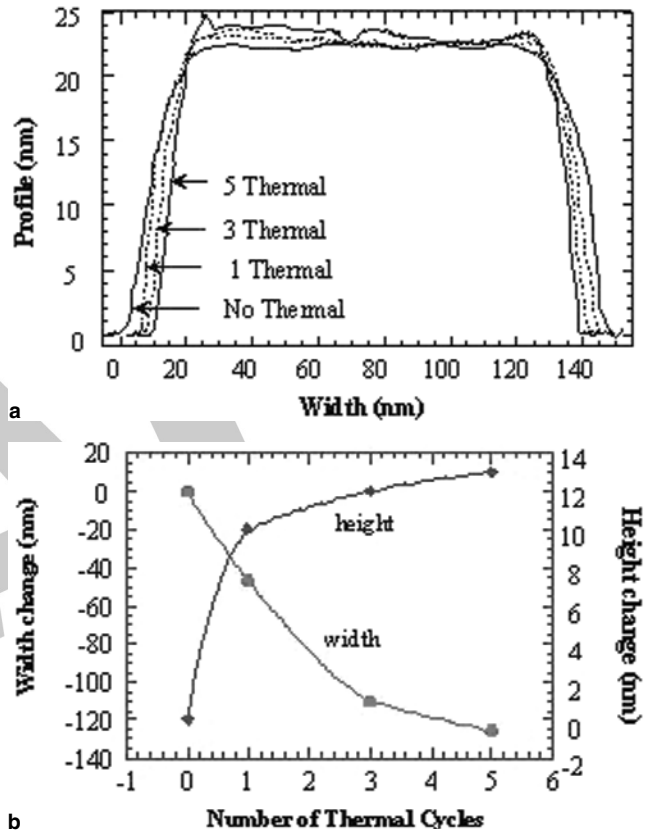

Fig. 7. (a) Typical profiles of a standalone Cu line prior to and following the first through fifth cycle between 293 K and 723 K. (b) Plot showing that the mean Cu line width decreased, whereas the mean Cu line thickness (height) increased progressively with thermal cycling.

DRAFT

and is accommodated at the interface by diffusional sliding, accounting for the 40–60 nm of lateral film shrinkage noted in Fig. 7 after 1 cycle. It will be shown that this very significant lateral shrinkage of Cu lines plays a crucial role in determining strain incompatibility between Cu and LKD across the vertical interfaces in BEIS.

Sliding at Cu/Ta/Low-K Dielectric Interfaces: Experiments

Figure 8 shows typical, surface AFM profiles of sample B (single-layer Cu/LKD structure) before and after cycling from 293 K to 723 K. Before cycling, a ~10-nm step was noted on the sample surface at the vertical Cu/LKD interfaces, indicating that the Cu lines were a little thicker than the LKD after CMP. After cycling, the interfacial step height (Δ) was found to change differently for different Cu line widths. This is shown in the surface step height versus probability plots in Fig. 9, which show that Δ increases with cycling for 1.8-μm-wide Cu lines, remains roughly unaltered for 0.8-μm lines, and decreases with cycling for 0.2-μm-wide lines. As noted in Fig. 7, the 1.8-μm Cu lines are expected to shrink appreciably in the IP direction.

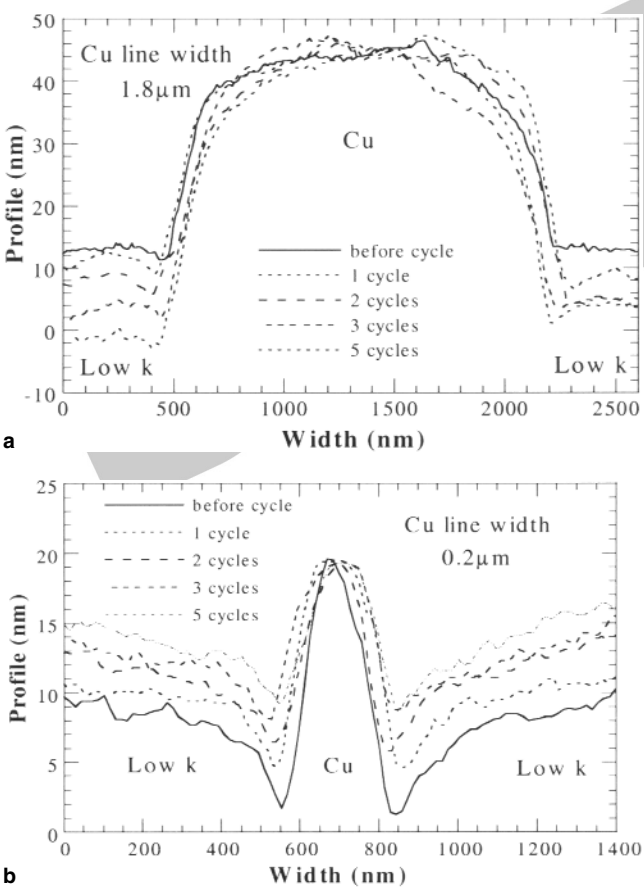

Fig. 8. The surface AFM profiles showing changes in interfacial step height between Cu and LKD during thermal cycling over 293–723 K. The low-K lines shrink in the OOP direction for wide Cu lines (a), leading to an increase in Δ, but expand relative to Cu for narrow Cu lines (b), resulting in a decrease in Δ.

The adjacent LKD lines are unlikely to be able to constrain this deformation because of the low Young's modulus of LKD (4–5 GPa) relative to Cu (130 GPa). Assuming that the vertical Cu/Ta/LKD interfaces are strongly bonded, the large lateral shrinkage of the Cu lines places the intervening LKD in IP tension, resulting in OOP shrinkage of the LKD because of the Poisson effect. Estimating the OOP Poisson's ratio of the LKD to be 0.2 and a 40-nm IP expansion of the 1.4-μm-wide LKD (i.e., 20-nm contraction of the 1.8-μm Cu line on each side) would result in OOP shrinkage of ~2 nm per cycle. When the OOP expansion associated with the IP contraction of the Cu lines is added to this OOP shrinkage of LKD, Δ can increase considerably, as observed in Fig. 9c.

On the other hand, when the Cu lines are only 0.2-μm wide, the IP shrinkage of the Cu line along the Cu/Si interface is very small, causing negligible IP strains in the adjacent LKD lines, which are quite wide (1.4 μm). However, the wide LKD lines are likely to apply significant OOP constraint on the narrow Cu because of the low CTE of LKD‡ relative to Cu, forcing the Cu lines to undergo compressive inelastic deformation in the OOP direction.§ Indeed, Cu films have been observed to creep significantly at temperatures above 323–343 K.[1,18] This permanent OOP shrinkage of Cu relative to LKD is consistent with the decrease of Δ after cycling observed in Fig. 9a. It should be noted that the observed shrinkage of Cu relative to LKD can also be rationalized by assuming OOP inelastic deformation of the LKD at high temperatures under the tensile constraint imposed by the Cu lines. However, this is incompatible with Fig. 9a, where the *wider* Cu lines would be expected to impose greater OOP tensile constraint and, therefore, cause greater expansion of the LKD relative to Cu, instead of the observed shrinkage. Therefore, OOP inelastic deformation of LKD does not appear to be an issue. In summary, for all Cu line widths, the OOP step height changes are driven by both IP and OOP deformation of Cu with the effects of IP deformation dominating for wide Cu lines, OOP deformation dominating for narrow Cu lines, and both effects having roughly equal but opposite contributions for Cu lines of intermediate width, as observed in Fig. 9b.

The observation that all changes in step height occur exactly at the interface (Fig. 8) suggests that the differential OOP deformation of Cu and LKD is accommodated at the interface by a sliding mechanism. This is illustrated by the edge profile of a Cu line before and after cycling up to 723 K, shown

‡ For the purposes of the present discussion, it is assumed that the OOP CTE of LKD is close to the IP CTE, which was measured to be $\sim 4.9 \times 10^{-6}$/K.

§ The origin of LKD constraint on the narrow Cu lines may be understood by visualizing the lines as thin Cu films of 0.2-μm thickness on a 1.4-μm-thick LKD substrate with the film plane normal to Si. Although the stiffness of LKD is small, its greater thickness enables it to constrain the OOP deformation of Cu.

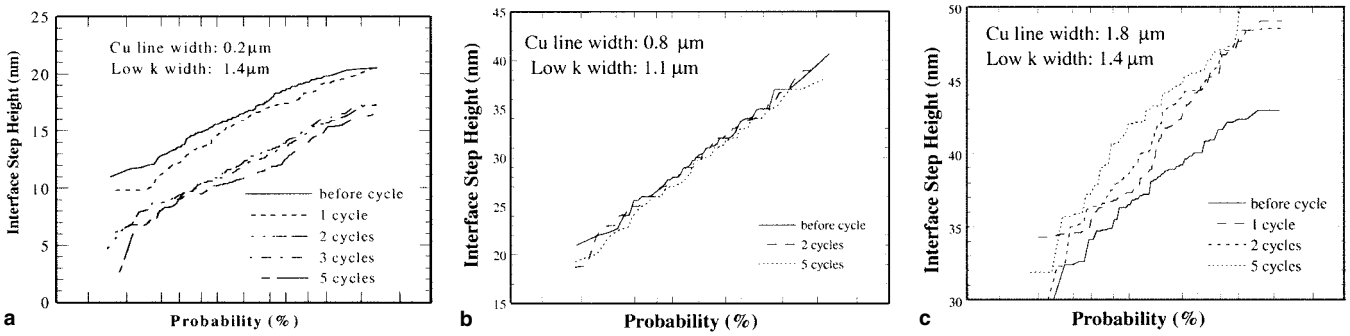

Fig. 9. The plots showing probability of change in the interfacial step height Δ at different stages of cycling over 298–723 K for 0.2-μm, 0.8-μm, and 1.8-μm-wide Cu lines. The Δ decreases for narrow Cu lines, increases for wide Cu lines, and remains relatively unaltered for Cu lines of intermediate width.

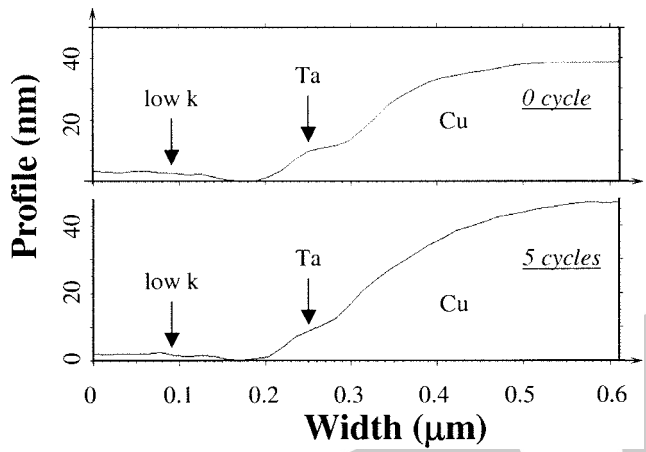

Fig. 10. A high-resolution AFM line profile across the Cu/Ta/LKD interface before and after five thermal cycles over 298–723 K in vacuum. The increased height difference between Cu and Ta after five cycles suggests that sliding actually occurs at the Cu/Ta interfaces.

in Fig. 10. The height difference between LKD and the Ta barrier layer is observed to remain constant, whereas the height difference between Ta and the Cu line changes upon cycling. This demonstrated that the differential deformation between Cu and LKD is accommodated by sliding at the Cu/Ta interface, consistent with the findings of Ref. 6. This sliding occurs by interface diffusion-controlled, diffusional creep; its kinetics being described by Eq. 1.

Figure 11a and b shows the surface profiles of a 0.2-μm-wide Cu line and the adjacent LKD at different stages of in-situ thermal cycling between 293 K to 398 K. Statistical analysis of approximately 100 such profiles at each temperature showed that between 293 K and 348 K no significant difference in the heights of Cu and LKD is noticeable, as observed in Fig. 11a. Between 348 K and 398 K, a very small OOP expansion (~1 nm) of the Cu line relative to the LKD is observed. After cooling back to 293 K, the interfacial step height (Δ) is smaller than that prior to cycling, as observed in Fig. 11b, indicating a net shrinkage of Cu relative to LKD. With continued cycling, Δ decreases steadily, with the mean Δ having decreased from 23 nm prior to cycling to ~21 nm after five cycles, as shown in the histogram in Fig. 11c.

These observations may be rationalized by Fig. 12, which shows a schematic of the cross section of the Cu/LKD structure on Si along with the stress states that drive sliding. During heating, the Cu line expands more in the OOP direction than the LKD line, placing the Cu in OOP compression. Although the Young's modulus of the LKD material is low relative to Cu ($E_{LKD} \sim 5$–7 GPa versus $E_{Cu} \sim 120$ GPa), the OOP compressive stress induced in the Cu line (σ_{Cu}) can be quite significant because of the much greater width of the adjacent LKD lines. Ignoring the effect of IP deformation of the Cu lines caused by the CTE mismatch between Cu and Si (reasonable because the Cu lines are very narrow), the OOP (vertical) stress in the Cu line in the absence of plastic relaxation may be approximated by a one-dimensional analysis as

$$\sigma_{Cu} = -\frac{(\alpha_{Cu} - \alpha_{LKD})\Delta T}{\left[\frac{1}{E_{Cu}} + \frac{1}{E_{LKD}}\left(\frac{w_{Cu}}{w_{LKD}}\right)\right]} \qquad (12)$$

where ΔT is the temperature change, and w_{Cu} and w_{LKD} are the widths of the Cu and LKD lines, respectively. For a 100-K rise in temperature, this gives $\sigma_{Cu} \sim -50$ MPa, which is enough to cause compressive creep of the Cu line in the OOP direction. Indeed, Cu films have been observed to creep significantly at stresses around 50 MPa at temperatures above 323–343 K.[1,19] Thus, the ~100-K thermal excursion in the present experiments causes noticeable permanent OOP shrinkage of Cu relative to LKD, which is accommodated by interfacial sliding, allowing the interfacial step height to decrease with thermal cycling. This sliding is driven by the interfacial shear stresses that arise because of the CTE mismatch between Cu and LKD and actually occurs at the vertical interfaces between the Cu line and the surrounding Ta liner, as shown in Fig. 10. It should be noted that the slight apparent extension of the Cu relative to LKD at 398 K is not due to interfacial sliding (Fig. 11a), because the sense of τ_i would result in a decrease in the step height, but

DRAFT

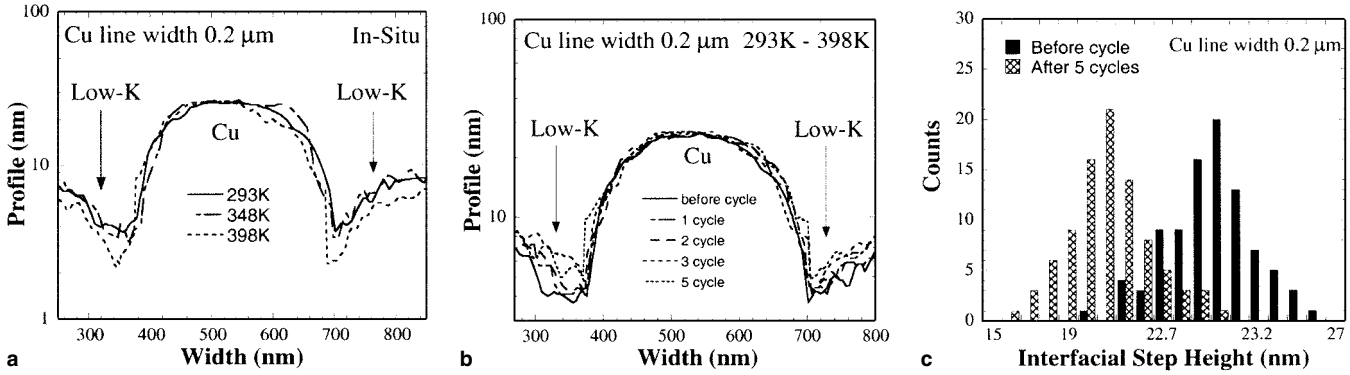

Fig. 11. The in-situ AFM surface profiles (a) during and (b) following thermal cycling over 293–398 K for a 0.2-μm-wide Cu line. Histograms of the interfacial step-height (Δ) distribution prior to cycling and after five cycles, showing a progressive decrease of Δ with cycling.

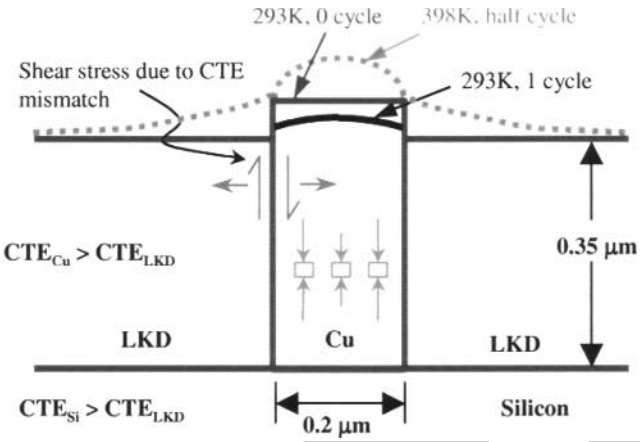

Fig. 12. A schematic showing relative OOP displacements of Cu/LKD at different stages of cycling between 293 K and 398 K. The corresponding stress states within the Cu line and at the Cu/LKD interface at the high temperature end of the cycle are also shown.

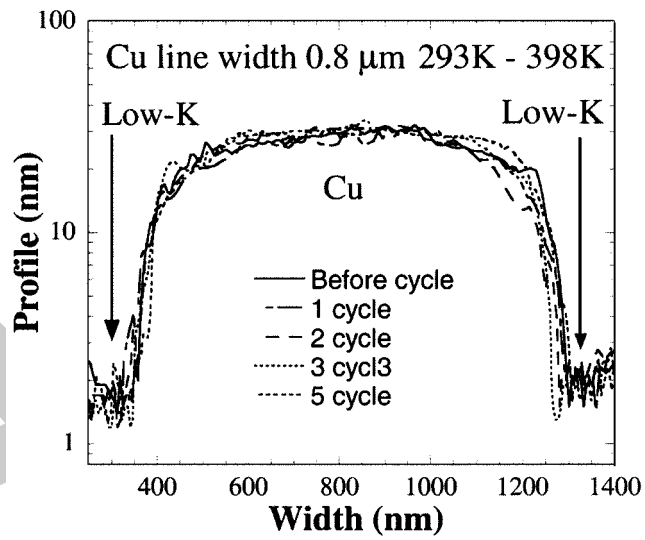

Fig. 13. The AFM surface profile of a 0.8-μm-wide Cu line and the adjacent LKD lines following thermal cycling between 293 K and 398 K, showing little change in the interfacial step height Δ caused by cycling.

rather caused by a strain gradient along the width of the Cu line.

Figure 13 shows the surface profile of a 0.8-μm-wide Cu line and the adjacent LKD following thermal cycling between 293 K and 398 K. In this case, little difference is noted in the step height after different number of cycles. As opposed to the 0.2-μm line, in this case, deformation and interfacial sliding in the IP direction (caused by CTE mismatch between Cu and Si) play an important role in determining the OOP step height. As shown previously, wide Cu lines may shrink appreciably in the IP direction following cycling. The adjacent LKD lines are unlikely to be able to constrain this deformation because of the low Young's modulus of LKD relative to Cu. The IP contraction of Cu is associated with OOP expansion caused by the Poisson effect, and this counteracts the OOP contraction of Cu relative to LKD caused by the CTE mismatch between Cu and LKD in the OOP direction. As a result, for the 0.8-μm-wide Cu line, no appreciable difference is noted in the interfacial step height following thermal cycling. This is consistent with Fig. 9, where Δ was noted to decrease for 0.2-μm Cu lines, remain relatively unaltered for 0.8-μm lines, and increase for 1.8-μm lines, with progressive cycling between 293 K and 723 K. Thus, for narrow lines, interfacial sliding is confined to the OOP interfaces, driven by τ_i generated because of the OOP CTE mismatch between Cu and LKD, whereas for wide lines, sliding occurs along both OOP and IP interfaces, with the sliding along IP interfaces being driven by τ_i because of the CTE mismatch between Cu and Si. In both cases, however, the actual sliding takes place at the Cu/Ta interface, which apparently acts a short-circuit diffusion path.[16,20]

In actual devices, the Cu/low-k layer is often capped with a thin dielectric layer (e.g., Si_3N_4). This layer may either constrain the OOP deformation noted in the present experiments or may be damaged itself because of the OOP sliding. This capping layer phenomenon is unclear and needs further study. It is generally well known that during thermal anneals, the surface of Cu lines undergo significant

grain-boundary grooving. This effect is likely to be convoluted with the OOP displacements noted here because of interfacial sliding. However, a grooving process operating at the Cu/Ta interface would invariably increase the thickness of the Cu lines by transporting matter from the vertical interfaces to the middle of the line. But, as shown earlier in our studies, we note that the thickness of the Cu lines relative to LKD may either increase or decrease because of thermal cycling, depending on the width of the Cu line. This strongly suggests that the effect noted here is dominated by OOP interfacial sliding with grain boundary grooving playing at best a second-order role.

Sliding at Vertical Cu/Ta/Low-K Dielectric Interfaces: Modeling Results

It is clear from the experimental results that in the interconnect structures previously discussed, sliding occurs along the Cu/Ta interfaces because of rapid interfacial diffusion of Cu, driven by the shear stresses that arise because of the CTE mismatch of Cu with Si or LKD and assisted by the smoothness of the interfaces. In these structures, the interfacial roughness parameter h (Eq. 1) is less than 1 nm, and because the interfacial sliding rate is proportional to h^{-3}, it is expected to be quite rapid. This is further aided by the presence of a tensile σ_n at vertical Cu/LKD interfaces, which is generated because of the lateral shrinkage of the Cu lines caused by sliding along the IP Cu/Si interfaces.

The interfacial step height Δ is determined by the kinetics of interfacial sliding, as well as the kinetics of creep of the thin-film Cu line. Here, we present the result of two sample computations based on the model outlined in the Model section and Fig. 5, using different values of the Cu grain size, d, (which influences the Cu creep rate according to Eq. 5b) and the interfacial creep pre-exponent $\delta_i D_{io}$ (Eq. 1). The computations are based on a Cu line width of 0.5 μm with adjoining LKD lines of 2-μm thickness on both sides. The results presented simulate one thermal cycle between 300 K and 400 K at the rate of 0.1 K/s, which is close to the experimental conditions of Fig. 11. Copper grain sizes of 0.1 μm and 0.5 μm are considered. Based on available data on Cu/LKD interfaces,[16] the activation energy for interfacial diffusion is assumed to be 67 kJ/mole. Because the value of $\delta_i D_{io}$ for the Cu/Ta interface is not known, it is assumed to be related to the grain-boundary diffusion pre-exponent for Cu, $\delta_{gb} D_{gbo}$ ($= 5 \times 10^{-15}$ m^3/s)[21] as

$$\delta_i D_{io} = C_i \cdot \delta_{gb} D_{gbo} \tag{13}$$

where C_i is a scaling constant. Two values of C_i (10^{-6} and 10^{-7}) are considered for the present calculations. The interfacial roughness, h, and the roughness-to-periodicity ratio, h/λ, (Eq. 1) are assumed to be 1 nm and 0.1, respectively. The other relevant Cu and LKD properties used in the calculations are listed in Table I.

Figure 14a and b shows the thickness variation of the Cu and LKD lines, as well as the evolution of the elastic and creep components# in the Cu line during thermal cycling over 300–400 K, for (a) d = 0.1 μm and $C_i = 10^{-7}$ and (b) d = 0.5 μm and $C_i = 10^{-6}$, respectively. The first set of conditions represents a rapidly creeping Cu line with a slowly creeping interface, whereas the second set represents a rapidly creeping interface with a slowly creeping Cu line. It is readily apparent that beyond about 350–360 K, the thicknesses of the Cu and LKD lines start diverging under both conditions, leading to a strain incompatibility between Cu and LKD, which is accommodated at the interface by sliding. For large d (slow Cu creep) and large C_i (rapid interface sliding), the LKD line expands whereas the Cu line shrinks (Fig. 14b). For small d and small C_i, on the other hand, both Cu and LKD shrink (Fig. 14a). In both cases, the Cu line undergoes a net shrinkage relative to LKD at the end of cycling, which is qualitatively consistent with the experimental trend observed in Fig. 11. However, as expected, the interfacial step that forms is more pronounced when the interfacial creep kinetics are larger (i.e., for greater C_i).

Interestingly, interfacial sliding can result in strain incompatibilities even when both Cu and LKD are elastic, as evidenced by Fig. 14b, where the Cu creep strain is negligible in the temperature range of interest. Because of the reduced creep and associated stress relaxation, however, the elastic strain range (and, therefore, the OOP normal-stress range) in the Cu line is larger in this case. This allows the shear stress at the vertical Cu/LKD interfaces (τ_i) to evolve differently during cycling. This is shown in Fig. 15, which plots the variation of τ_i with distance from the Si surface (x) normalized by the initial line thickness (w/2) at various stages of cycling. Figure 15a corresponds to the interfacial and Cu creep conditions of (a), whereas Fig. 15b corresponds to condition (b). In both cases, τ_i starts out being zero at 300 K, because there are no thermal stresses at the beginning of cycling, and begins to increase in magnitude as the temperature is increased. It is readily apparent that under condition (a), τ_i has the same sign at all stages of cycling, whereas under condition (b), the signs of τ_i are opposite during heating and cooling. It is this switching of the sign of τ_i during cycling that is responsible for the observed LKD expansion and Cu contraction under condition (b), as opposed to both LKD and Cu contracting, albeit differentially, under condition (a). Thus, the operative deformation mechanism and kinetics of both the interface and the lines are important in determining the interfacial strain incompatibilities produced between Cu and LKD during thermal cycling.

Although the model accounts for linear-hardening plasticity of Cu, under the temperature range and rate conditions used here, the Cu lines do not undergo plastic deformation.

DRAFT

Table I. Properties and Constants Used in Calculation

	Copper	LKD
Melting temperature, T_m (K)	1,356	N/A
Coefficient of thermal expansion (1/K)	18×10^{-6}	4.9×10^{-6}
Young's modulus at 300 K (GPa)	115	7
Shear modulus at 300 K (GPa)	40	—
Work hardening coefficient at 300 K, K_{1_o} (MPa)	1,000	—
Temperature dependence for modulus calculations	$\Delta = (T_m/G_f)(dG_f/dT) - 0.54$	
Temperature-dependent yield strength of Cu (MPa)	$\sigma_{ys} = 300 \exp[-7(T - 296)/700]^2$	
Temperature-dependent Young's modulus	$E_f = E_{fo}(1 + \Delta(T - 300)/T_m)$	
Temperature-dependent shear modulus	$G_f = G_{fo}(1 + \Delta(T - 300)/T_m)$	
Temperature-dependent linear hardening modulus	$K_1 = K_{1_o}(1 + \Delta(T - 300)/T_m)$	
Frequency factor for lattice diffusion, D_{lo} (m^2/s)	2×10^{-5}	
Activation energy for lattice diffusion, Q_l (J/mole)	197,000	
Pre-exponential for grain boundary diffusion, $\delta_{gb}D_{gbo}$ (m^3/s)	5×10^{-15}	
Activation energy for grain boundary diffusion, Q_{gb} (J/mole)	104,000	
Atomic volume, Ω (m^3)	1.18×10^{-29}	
Copper grain size, d (μm)	0.1 or 0.5	
Cu line width, $2t_f$ (μm)	0.5	
LKD line width, ts (μm)	10	

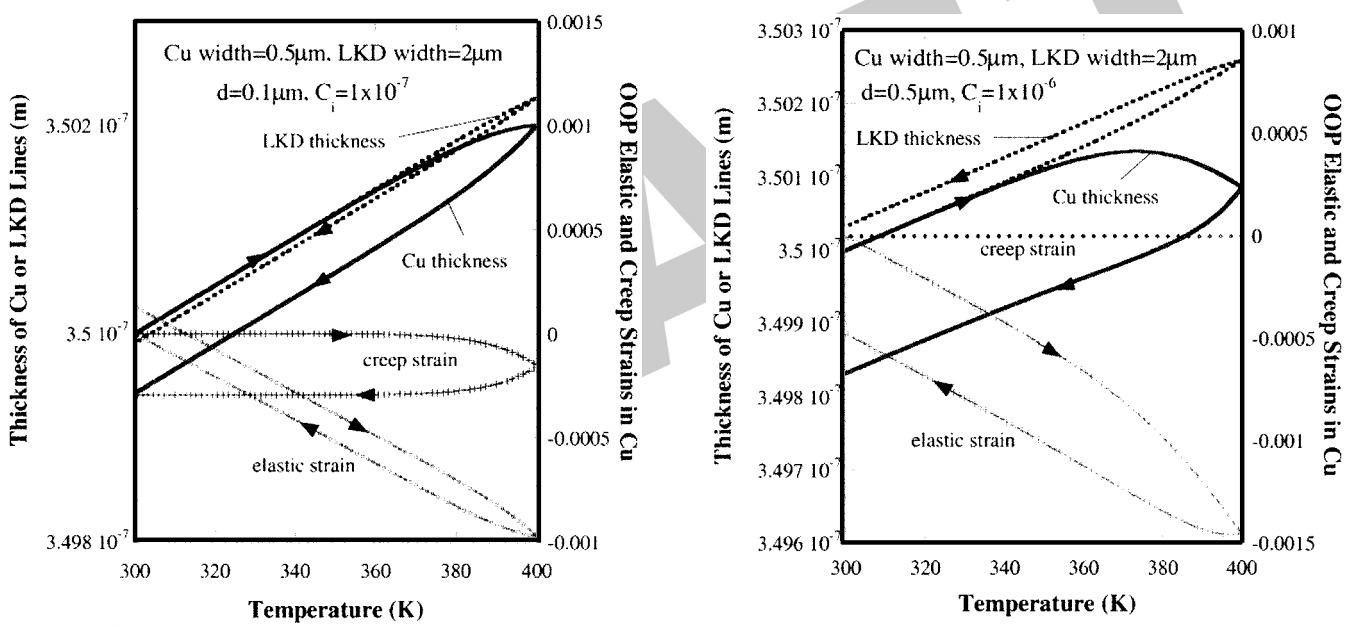

Fig. 14. A variation of Cu and LKD line thickness and associated Cu strains in the OOP direction during thermal cycling over 300–400 K for two different sets of material properties: (a) rapid Cu creep and slow interfacial creep and (b) slow Cu creep and rapid interfacial creep.

Deformation of Back-End Interconnect Structures under Far-Field Packaging Stresses

In addition to the effects of chip-level stresses previously discussed, very large package-level shear stresses are induced in the BEIS when a Si device joined to an organic substrate is thermally cycled. These stresses increase with increasing IP distance from the center of the chip (i.e., distance from the neutral point) and may be large enough to cause large-scale plasticity of the Cu lines because the compliant LKD offers little mechanical constraint. This effect was studied using the sample and fixture shown in Figs. 4a and b. During in-situ cycling in the AFM, the cross section of a 0.5-μm Cu line was observed, and the locus of points along the perimeter of the line at an elevation of 20 nm from the adjacent regions (Si or LKD) were recorded, as shown in Fig. 16. It is seen that the line undergoes significant shear distortion during heating to 398 K, much of which remains upon cooling to 298 K, demonstrating that the line is plastically deformed. After 25 cycles, a net shear strain of ~0.15 is observed to have accrued in the Cu line. This is consistent with the phenomenon of film crawling during thermal cycling, where Al lines on Si were noted to deform in shear with the strain ratcheting up with an increasing

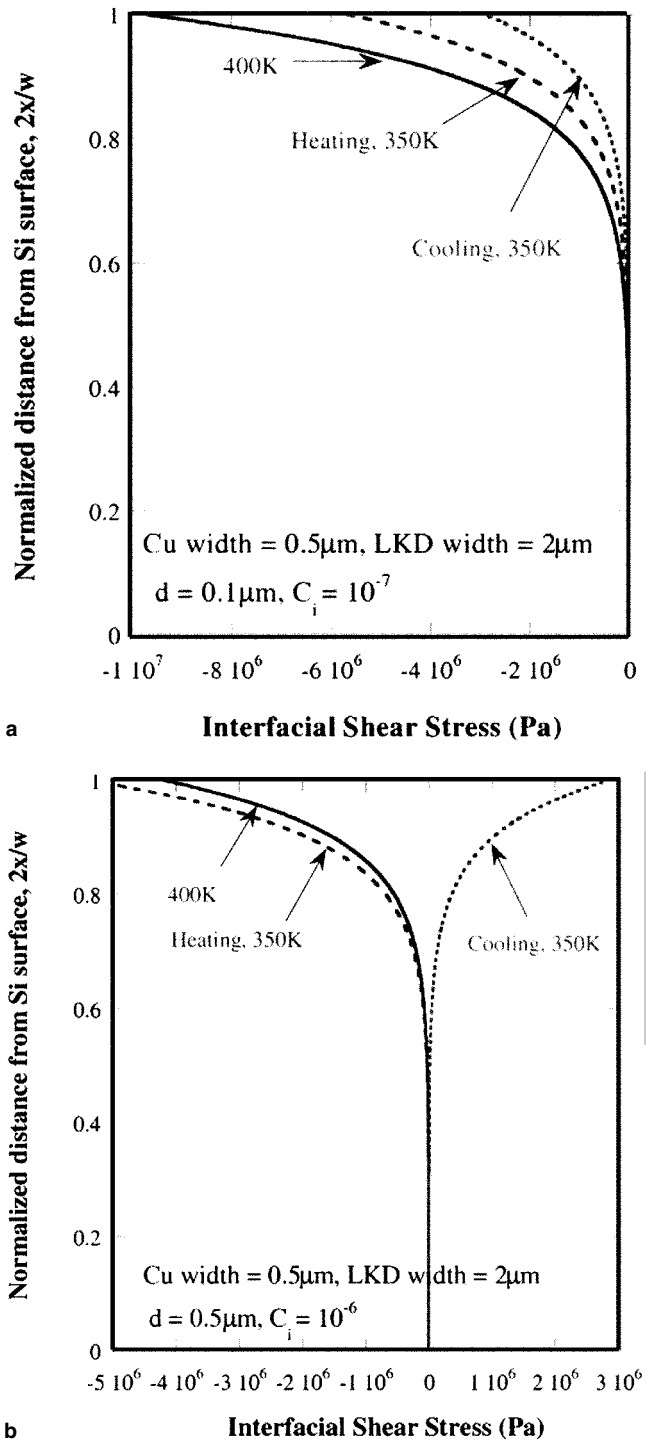

Fig. 15. The interfacial shear-stress (τ_i) distribution along the OOP direction at different stages of thermal cycling over 300–400 K for two different sets of material properties: (a) rapid Cu creep and slow interfacial creep and (b) slow Cu creep and rapid interfacial creep. Prior to the start of cycling, τ_i is zero at all locations on the Cu/LKD interface because the lines are nominally stress free.

number of cycles, eventually breaking a SiN barrier layer surrounding the line.[5] It is possible that similar effects may be observed in the present system after numerous cycles with the distorted Cu line breaking the Ta barrier layer and migrating

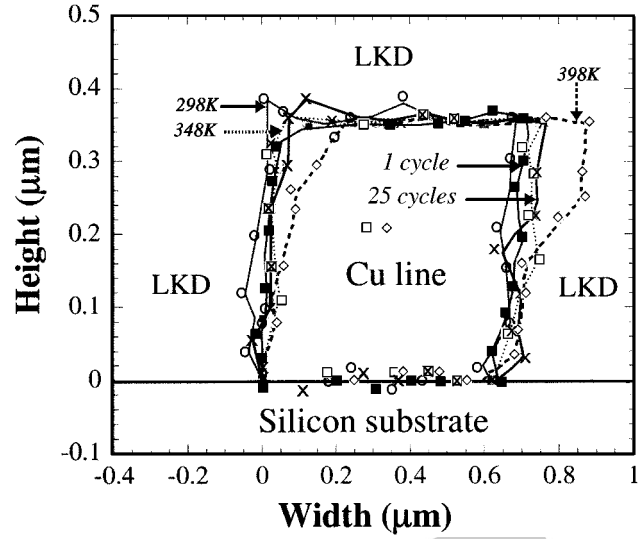

Fig. 16. The perimeter of a cross section of a 0.5-μm wide Cu line embedded in LKD at different stages of thermomechanical cycling between 298 K and –398 K with the sample mounted in the bimetallic fixture. During cycling, a nominal shear strain of 0.5–1 was imposed on the back-end structure to simulate the effect of far-field package-level stresses.

laterally relative to Ta via interfacial creep. The inability of the LKD to constrain such migration makes this a likely failure mechanism in Cu/LKD BEIS.

CONCLUSIONS

Thermal cycling resulted in lateral shrinkage of standalone Cu thin-film lines on Si, along with a change in edge profile. This was attributed to IP inelastic deformation of the Cu line, accommodated by sliding at the Cu/Ta interface via interfacial diffusion-controlled diffusional creep. Lateral Cu-line shrinkage along with OOP CTE mismatch between Cu and the adjacent LKD also provided the driving force for OOP interfacial sliding, which accentuated steps on CMP single-layer Cu/low-K BEISs. Following ex-situ cycling over 293–723 K, the OOP dimension (i.e., thickness) of narrow Cu lines (0.2-μm wide) decreased relative to the adjacent dielectric lines, whereas the thickness of wide Cu lines (1.8-μm wide) increased relative to the dielectric. This difference is attributable to the different contributions of IP deformation and sliding at the horizontal Cu/Si interfaces and OOP deformation and sliding at the vertical Cu/LKD interfaces in the two cases. In all cases, the actual sliding occurred at the interface between Cu and the Ta barrier layer, although the driving force was provided by CTE mismatch between Cu and Si or Cu and LKD. Similar results were noted during in-situ thermal cycling experiments in an AFM equipped with an environmentally protected hot stage.

A micromechanical model for computing the OOP deformation of Cu and LKD, incorporating the effects of interfacial sliding based on a modified shear-lag approach, is presented. Sample computa-

AFT

tions showed that the model is able to capture the qualitative trends observed experimentally via the in-situ hot-stage AFM studies. Interestingly, the modeling effort demonstrated that interfacial steps can appear in planarized Cu/LKD structures even when there is no plasticity or creep of the Cu or LKD lines.

In-situ AFM measurements were conducted on the cross section of back-end structures under conditions of thermal cycling with superimposed far-field thermomechanical stresses in order to simulate the effect of package-level stresses on the stability of the Cu-LKD structure. It is shown that Cu lines embedded in mechanically compliant LKD can undergo significant permanent shear deformation, which increases progressively with cycling, potentially posing a long-term reliability problem.

ACKNOWLEDGEMENTS

This work was supported by NSF Grant No. DMR-0075281. The authors are grateful to Drs. J. Molla and V. Wang, Motorola, for providing the samples for this investigation and Dr. Burt Fowler for his encouragement and support.

REFERENCES

1. M.D. Thouless, J. Gupta, and J.M.E. Harper, *J. Mater. Res.* 8, 1845 (1993).
2. M.W. Chen and I. Dutta, *Appl. Phys. Lett.* 77, 4298 (2000).
3. I. Dutta, M.W. Chen, K. Peterson, and T. Shultz, *J. Electron. Mater.* 30, 1537 (2001).
4. I. Dutta, K. Peterson, and M.W. Chen, *Proc. 9th Int. Symp. Plasticity*, ed. S. Khan and O. Lopez-Pamies (Fulton, MD: NEAT Press, 2002), pp. 117–119.
5. M. Huang, Z. Suo, and Q. Ma, *Acta Mater.* 49, 3039 (2001).
6. D.V. Zhmurkin, T.S. Gross, and L.P. Buchwalter, *J. Electron. Mater.* 26, 791 (1997).
7. M. Gosz and A.F. Okyar, *Mech. Mater.* 31, 317 (1999).
8. L.M. Gignac, K.P. Rodbell, C. Cabral, P.C. Andricacos, P.M. Rice, R.B. Beyers, P.S. Locke, and S.J. Klepeis, *Mater. Res. Soc. Symp.* 564, 373 (1999).
9. W.D. Nix, *Metall. Trans. A* 20A, 2217(1989).
10. A. Kelly, *Strong Solids*, 2nd ed. (Oxford, U.K.: Oxford University Press, 1973), ch. 5.
11. H.L. Cox, *Br. J. Appl. Phys.* 3, 122 (1952).
12. J.V. Funn and I. Dutta, *Acta Mater.* 47, 149 (1999).
13. K.A. Peterson, I. Dutta, and M.W. Chen, *Scripta Mater.* 47, 649 (2002).
14. K.A. Peterson, I. Dutta, and M.W. Chen, *Acta Mater.* 51, 2831 (2003).
15. R. Raj and M.F. Ashby, *Metall. Trans.* 2, 1113 (1971).
16. P.S. Ho, K.D. Lee, E.T. Ogawa, X. Lu, H. Matsuhashi, V.A. Blaschke, and R. Augur, *Proc. Int. Electron Dev. Meeting* (Piscataway, NJ: IEEE, 2002), pp. 741–744.
17. I. Dutta, *Acta Mater.* 48, 1055 (2000).
18. S.H. Lau, S. Huang, and A. Koo, *Semicond. Int.* 23, 239 (2000).
19. P.A. Flinn, *J. Mater. Res*. 6, 1498 (1991).
20. K.A. Peterson, C. Park, and I. Dutta, *MRS Symp. Proc.* 716, 483 (2002).
21. H.J. Frost and M.F. Ashby, *Deformation Mechanism Maps—Plasticity and Creep of Metals and Ceramics* (Oxford, U.K.: Pergamon Press, 1982).

DRAFT

Annotations from 884S11.pdf

Page 3

Annotation 1; Label: IPC; Date: 9/5/2003 3:14:03 PM
Location of vendor?

Page 4

Annotation 1; Label: IPC; Date: 9/5/2003 3:14:16 PM
Is the indicated math okay as set?

Annotation 2; Label: IPC; Date: 9/5/2003 3:14:27 PM
Vendor name and location?

Page 6

Annotation 1; Label: IPC; Date: 9/5/2003 3:14:46 PM
Vendor name and location?

Page 11

Annotation 1; Label: IPC; Date: 9/5/2003 3:15:15 PM
Please provide a column head for the first column in Table I.

Page 13

Annotation 1; Label: IPC; Date: 9/5/2003 3:15:36 PM
Reference 4: Is this entry set correctly?

Annotation 2; Label: IPC; Date: 9/5/2003 3:15:56 PM
Reference 10: Is this entry set correctly? Opening and closing page numbers?

Online Proofing Guidance Page

FIRST STEP:

Install Adobe Acrobat Reader if you do not already have this or another Acrobat product installed on your computer. You can do this free of charge by connecting to the Adobe site and following the instructions at:

http://www.adobe.com/products/acrobat/readermain.html

SECOND STEP:

Please download and print your PDF file — we recommend that you save this file to disk, rather than opening it from within your Browser.

From a PC:

1. Right-click on the file/article link.
2. Select ''Save Target as''
3. Select a desired location on your computer to save the file to, and click on ''Save''
4. Open your PDf file directly with Acrobat Reader or another Acrobat product.
5. Print this file as you normally would with any typical application. Example: Go up to your toolbar, select ''File'', select ''Print''.

From a MAC:

1. Hold the mouse button down over the link.
   a. In Internet Explorer, select ''Download Link to Disk'' from the resulting pop-up menu
   b. In Netscape, select ''Save this Link as'' from the resulting pop-up menu
2. Select a desired location on your computer and click on ''Save''
3. Open your PDF file directly with Acrobat Reader or another Acrobat product.
4. Print this file as you normally would with any typical application. Example: Go up to your menu bar, select ''File'', select ''Print''.

THIRD STEP:

Please go through the file you have just printed and thoroughly and clearly mark any revisions you would like to see implemented in your paper. If you have had any changes in phone/fax or e-mail addresses since your paper was submitted, please send us this new information.

FOURTH STEP:

Your revised paper needs to be faxed or mailed to:

IPC Print Services
Attn: Sheryl Dickenson
501 Colonial Drive
St. Joseph, MI 49085
Fax number: 1-269-983-4064

If you have questions regarding your paper in general, you may email or telephone:

IPC Print Services
Attn: Sheryl Dickenson
Email: sdickens@ipcjci.com
Phone: 1-269-983-7412, ext. 529